# Range-Doppler Imaging Approach for the Wireless Reading of Mechanical Sensors

Dominique Henry, Patrick Pons, Hervé Aubert

# Range-Doppler Imaging Approach
# for the Wireless Reading of Mechanical Sensors

Dominique Henry[1], Patrick Pons[1], and Hervé Aubert[1,2]

[1]MINC dept, LAAS-CNRS, Toulouse, France
[2]Toulouse University, France

## Abstract

We investigate in this paper the wireless interrogation of chipless and passive mechanical sensors using a range-Doppler imaging algorithm. As an example, a Crookes radiometer illuminated by a light of controlled illuminance is interrogated by using a 24GHz FM-CW radar. A remote detection algorithm is proposed to estimate the reading range and Doppler harmonics embedded in the electromagnetic signal backscattered by the radiometer. From these harmonics the accurate estimation of illuminance is achieved for long reading ranges of at least 3.5m in a cluttered environment.

**keywords** : chipless sensor, mechanical sensor, radar imagery, range-Doppler, remote sensing, wireless sensor, zero-power sensor.

## 1 Introduction

Wireless and chipless sensors are a relevant solution for remotely interrogating and sensing physical quantities, especially when batteries cannot be replaced easily, such as for structural health monitoring applications, or where using electronic devices is critical, for example in harsh environments. To achieve the wireless interrogation of such sensors, various technologies can be considered using Radio Frequency Identification (RFID) tags (see e.g.,[1]) or fully-passive sensing devices remotely interrogated by radar readers [2]. Beside short interrogation range of typically few ten centimeters, RFID tags often require an increased coding capacity to be efficient [3]. Longer reading range can be achieved from using harmonic radars [4], but this technology requires high power-consuming frequency transposition by using a nonlinear device in the tag. Other technologies include useful Surface Acoustic Wave tags for the remote sensing in extreme conditions [5]. However, achieving reading range of more than few meters remains very challenging from using this well-documented technology. The authors of the present study investigated an alternative solution. It consists

of using of millimeter-wave radar imagery technique for the long-range interrogation of chipless and passive (or *zero-power*) sensors. This approach allows remotely identifying and reading sensors at a range of tenth of meters in cluttered environments [6]. However, it requires the use of delay lines for mitigating the electromagnetic clutter, and it needs the challenging design and fabrication of electromagnetic transducers operating in the millimeter-wave frequency band.

In this paper, we investigate the feasability of another solution for chipless sensors based on mechanical transduction. Such mechanical sensor consists of mobile sensing structures with no integrated circuit and no power supply. Sensors based on sub-wavelength displacement of matter [7] or fluid [8] have been proposed as an alternative solution to the electromagnetic transduction. In this paper, using a range-Doppler imaging technique, we propose to use mechanical sensors with much larger mobile constitutive parts for the remote detection and wireless reading of physical quantities in stationary cluttered environments. The very first example of such sensor studied here is a Crookes radiometer with 4 pans, which rotate thanks to the so-called *thermal diffusion* effect [9]. This physical effect is still of scientific interest today [10]. A 24GHz Frequency-Modulated Continuous-Wave (FM-CW) radar interrogates the rotating structure of few centimeters size. We show that the range-Doppler frequencies derived from radar images allows remotely estimating the reading range of the Crookes radiometer and the rotation speed of the pans when illuminated by a light. From the remote measurement of this rotation speed, the illuminance is derived. Detection of rotating targets from radar imaging technique is generally used in aeronautics and defence applications [11]. We extend it to the long-range wireless interrogation of the Crookes mechanical sensor for the remote measurement of the illuminance in cluttered environments. Application to the long-range reading of other kind of chipless mechanical sensors could be investigated.

The paper is divided in two sections. The first section describes the measurement principle. The FM-CW signal backscattered by a stationary rotating target and its Doppler harmonics specifically generated by the metallic pans rotation are rigorously simulated for various incident linearly polarized plane wave. Next, a range-Doppler imaging algorithm is applied for estimating from a range-Doppler imaging algorithm both the radar-to-sensor distance and the rotation speed of the pans for multiple controlled light illuminances. Material and methods are exposed in the second section. The reading range as well as the illuminance of light are finally derived from measured radar data in an anechoic chamber and in a cluttered environment.

## 2   Measurement Principle

### 2.1   Basics on Signal Processing of FM-CW Radar Data

A FM-CW radar is used for remotely interrogating a stationary mechanical chipless sensor. The FM-CW radar transmits a frequency modulated signal, so called *chirp*, at the carrier frequency $f_c$ and with the modulation bandwidth

$B$. The shape of the frequency modulation is here a *saw-tooth* signal with the up-ramp duration $T_{up}$. Successive chirps are transmitted with the repetition time (or *pulse repetition interval*) denoted by $T_{rep}$ ($> T_{up}$). Let $\alpha_c = \frac{B}{T_{up}}$ be the *frequency sweep rate*. The radar-to-sensor distance is denoted by $R$ and the round trip duration $\tau$ of the electromagnetic signal backscattered by the sensor is given by $\tau = \frac{2R}{c}$, where c designates the vacuum speed of light. From the mixing and filtering of the transmitted and received signals, the radar delivers the following signal $s(t)$ at time $t$ (see e.g., [12]):

$$s(t) = K.exp\{2j\pi(f_c\tau + \alpha_c t\tau - \frac{1}{2}\alpha_c\tau^2)\} + \mathcal{N}(t) \qquad (1)$$

where $K$ designates the signal magnitude and $\mathcal{N}(t)$ models eventual additive noise. The sampled version $s(n)$ of this signal is then given by:

$$s(n) = K.exp\{2j\pi(f_c\tau + \alpha_c\frac{n}{N}T_{up}\tau - \frac{1}{2}\alpha_c\tau^2)\} + \mathcal{N}(n) \qquad (2)$$

where $N$ is the number of signal samples during the period $T_{up}$ and the natural number $n$ ($0 \leq n < N$) represents the so-called *fast time* index. Let $\sigma(t)$ be the Radar Cross Section (RCS) of the mechanical chipless sensor at time $t$. We assume here that slow variations over time of the RCS occur during the radar up-ramp duration $T_{up}$. The signal magnitude $K$ defined in eq. (2) is then no more constant and varies slowly over time. Based on the linear simplified model, the magnitude $K(t)$ of the signal $s(t)$ delivered by the radar can be approximated as follows:

$$K(t) = K_0\sqrt{\frac{P_t G_t \sigma(t) A_{eff}}{(4\pi R^2)^2}} \qquad (3)$$

where $P_t$ is the transmitted power, $G_t$ is the gain of the (impedance matched) transmitting radar antenna, $K_0$ is a constant (which depends on the power gain of the radar receiver channel) and $A_{eff}$ denotes the effective area of the radar receiving antenna. If the radar transmits $M$ consecutive chirps, the sampled signal can be rewritten in the following matrix form:

$$S(m, n) = K(mT_{rep}).f(n) + \mathcal{N}(m, n) \qquad (4)$$

where the natural number $m$ ($0 \leq m < M$) represents the *slow time* index and, according to eq. (1), $f(n) = exp\{2j\pi(f_c\tau + \alpha_c\frac{n}{N}T_{up}\tau - \frac{1}{2}\alpha_c\tau^2)\}$ with $0 \leq n < N$. To estimate the reading range of the chipless mechanical sensor, the Discrete Fourier Transform (DFT) of size $N$ is applied on the fast time dimension of $S(m, n)$ as follows:

$$S_{DFT}(m, n_2) = DFT\{S(m, n)\} \qquad (5)$$

where the natural number $n_2$ ($0 \leq n_2 < \frac{N}{2}$) denotes the range index. As the theoretical depth resolution $d$ is given by $d = \frac{c}{2B}$ [13], the predicted maximal readable range is then given by $R_{max} = \frac{N.d}{2}$. To derive the range-Doppler image

3

from the radar measurement [14], the DFT of size $M$ is applied to the slow time dimension of $S_{DFT}(m, n_2)$, that is:

$$S_{2,DFT}(m_2, n_2) = DFT\{S_{DFT}(m, n_2)\} \qquad (6)$$

where the natural number $m_2$ ($-M/2 \leq m_2 < M/2$) denotes the Doppler frequency index. The Doppler frequency resolution $\delta_f$ is given by $\delta_f = \frac{1}{M.T_{rep}}$ and the measurable Doppler frequency $f_m$ ranges from $-\frac{1}{2.T_{rep}}$ to $\frac{1}{2.T_{rep}}$.

## 2.2 Electromagnetic Simulation of the Rotating Mechanical Sensor

We simulate in this section the range-Doppler response of a mechanical sensor composed of four metallic pans that rotate around a stationary axis. This sensor is derived from the Crookes radiometer. Each pan is a square of size $a$=2cm separated from each other by the angle of $\frac{\pi}{2}$ around the z-axis. The azimuth angular speed is denoted by $\omega$ (=0.5 rad/s). The shortest distance $b$ between two opposite pans is of 0.5cm. The rotating pans are located at the radar-to-sensor distance $R$ of 4m. The radar transmits $M$=1024 chirps with the repetition time $T_{rep}$=30ms. The carrier frequency $f_c$ of the chirp is of 24GHz and the modulation bandwidth $B$ is of 1GHz. The theoretical depth resolution $d$ is then of 15cm. The duration $T_{up}$ of the up-ramp is 50$\mu$s and the number of signal samples $N$ is 256. $\mathcal{N}(t)$ is assumed to be a white Gaussian noise with the standard deviation of 0.1V and zero mean. The transmitted power $P_t$ is set to 100mW while $G_t$=8dBi and $A_{eff}$=1m$^2$.

The RCS of the rotating structure has been rigorously simulated by using the Finite Element Method solver HFSS. In this simulation, the time-harmonic vertically polarized (V-polarized) incident plane wave at 24GHz is generated in the elevation plane $\theta$=0° for an azimuth angle ranging from 0 to $2\pi$ with a resolution of 1°. Two configurations are simulated:

- In the first configuration, the four pans are tangential to the V-polarized incident electric field, as illustrated in Fig. 2.2. The simulated RCS is displayed in Fig. 2.2 between 0 and $2\pi$ in the elevation plane. As expected the RCS pattern has a $\frac{\pi}{2}$-rotational symmetry. The half-power beamwidth of the main lobes at $\varphi \equiv 0[\frac{\pi}{2}]$ is of 3° and we observe two high amplitude sidelobes. These lobes are apparent when two opposite pans are normal to the wavenumber direction of the incident electric field. The half-power beamwidth of the main lobes at $\varphi \equiv \frac{\pi}{2} [\frac{\pi}{2}]$ is of 22° and are generated by the dihedral corners formed by two tangential metallic pans;

- In the second configuration, the four pans are inclined by the angle $\Delta\theta$=5° to the incident electric field polarization, as shown in Fig. 2.2. However, the axis of rotation is still tangential to the incident electric field. The simulated RCS is displayed in Fig. 2.2. Compared with the first configuration, the $\frac{\pi}{2}$-rotational symmetry of the RCS pattern is replaced by the
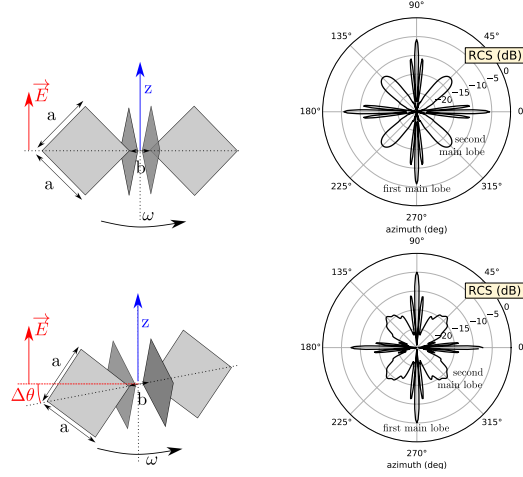
4

Figure 1: Schematic of the mechanical chipless sensor composed of 4 rotating metallic pans (a) tangential or (c) inclined to the incident electric field polarization ($a$=2cm and $b$=0.5cm). Simulated RCS of (b) tangential or (d) inclined 4 metallic pans for the incident V-polarized electric field at 24GHz in the elevation plane $\theta$=0°.

$\pi$-rotational symmetry. Magnitudes of two of the first main lobes ($\theta$=0 and $\theta$=$\pi$) decrease by 2.5dB due to the 5° inclination of the normal pans.

In order to simulate the rotation of the four metallic pans, the computed RCS patterns presented above are sampled into $M$=1024 samples with angular resolution $\Delta\omega \equiv m\omega T_{rep}$ [$2\pi$]. The rotational frequency of modes are given by $f_k=\frac{k\omega}{2\pi}$, where $f_1=\frac{\omega}{2\pi}$ is the fundamental rotational frequency of the pans. The range-Doppler signal is then computed according to the equations reported in Section 2.1. In Fig. 2 are displayed the range-Doppler signal at the range index $m_2$=27, which corresponds approximately to the sensor location. Results are given when four pans are tangential to the incident electric field (first configuration) and when the four pans are inclined by 5° to the electric field polarization (second configuration). The frequency resolution of these spectra is $\delta_f$=3.2E-2Hz. In the first configuration, the two lower frequency peaks are $f_4=\frac{2\omega}{\pi}$=0.31Hz and $f_8=\frac{4\omega}{\pi}$=0.62Hz. Because of the $\frac{\pi}{2}$-rotational symmetry of the pans, $f_1$ and $f_2$ do not correspond to peaks in the simulated spectra. However the highest peak is $f_8$ (magnitude of -32.5dB) due to the $\frac{\pi}{8}$ angle between each main lobes. In the second configuration, the first frequency peak is $f_2=\frac{\omega}{\pi}$=0.18Hz with the magnitude of -42.8dB because of the $\pi$-rotational symmetry of the rotating structure. Moreover, the magnitude of the $f_8$ peak decreases (-37.0dB) and the peak at frequency $f_4$ is very low (-54.3dB). In both cases, peaks at frequency $f_6$ are not easily distinguishable. Therefore, the mechanical sensor generates specific Doppler harmonics that directly depend on the inclination angle $\Delta\theta$.
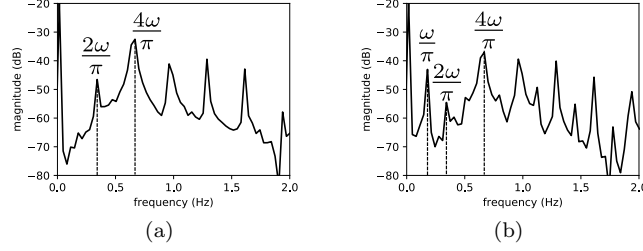
5

Figure 2: Simulated Doppler spectrum of the rotating metallic pans at the range index $m_2$=27 and angular speed $\omega$=0.5 rad/s for the 4 rotating metallic pans: (a) first configuration and (b) second configuration with the inclination angle of $5°$.

## 2.3 Range-Doppler Algorithm

We propose an algorithm to estimate the range of the interrogated mechanical sensor presented in Section 2.2, and to remotely determine the Doppler harmonics. The algorithm is decomposed into the following 8 steps (see Fig. 3):

*(i)* Raw data are first recorded. The signal $s(t)$ given in eq. (2) is the average of successive mixed signals that are sampled during four up-ramps of duration $T_{up}$=50$\mu$s. This average is performed with the repetition time $T_{rep}$=30ms for $M$=2000 successive signals $s(t)$;

*(ii)* and *(iii)* The matrix $S(m, n)$ defined in eq. (4) is built and the singular value decomposition is performed on matrix $S$ along the fast time axis. The 0Hz-frequency peak generated by the stationary target is removed by replacing the first singular value $\sigma_1$ of the matrix $\Sigma$ by zero. Removing the 0Hz-frequency peak might be necessary when computing the mean Doppler echo level (see step *(v)*);

*(iv)* As described in eq. (5) and (6), the range-Doppler transform is applied on the matrix $S'(m, n)$. Positive range indexes $n_2 \geq 0$ are selected. The theoretical depth resolution is $d$=15cm and the frequency resolution is $\delta_f$=3.2E-2 Hz;

*(v)* For each range index $n_2$, a peak detection algorithm is applied to positive Doppler frequencies ($0 \leq m_2$). The minimal frequency distance between two peaks is $\delta_{min}$=0.1Hz. The minimal threshold level for detecting peaks is $\Delta_{th}$=$\langle S_{2,DFT}(n_2)\rangle$ + 10dB, where $\langle S_{2,DFT}(n_2)\rangle$ is the mean value of $S_{2,DFT}$ at the range index $n_2$ for positive indexes $0 \leq m_2 < \frac{M}{2}$. Because the 0Hz-frequency peak is removed in step *(iii)*, it has no influence on the computed mean value;

*(vi)* We select harmonics among the detected peaks for each range index $n_2$ and we define a selection criterion $G(f_{p,n_2})$ representing the number of harmonics of the frequency $f_{p,n_2}$ at the range index $n_2$;

*(vii)* We assume that the Doppler spectrum obtained at the estimated radar-to-sensor distance contains the maximal number of detected harmonics. The radar-to-sensor distance is finally determined at the range where the maximal number of harmonics has been detected;

*(viii)* Once the radar-to-sensor distance is estimated, harmonics in the signal
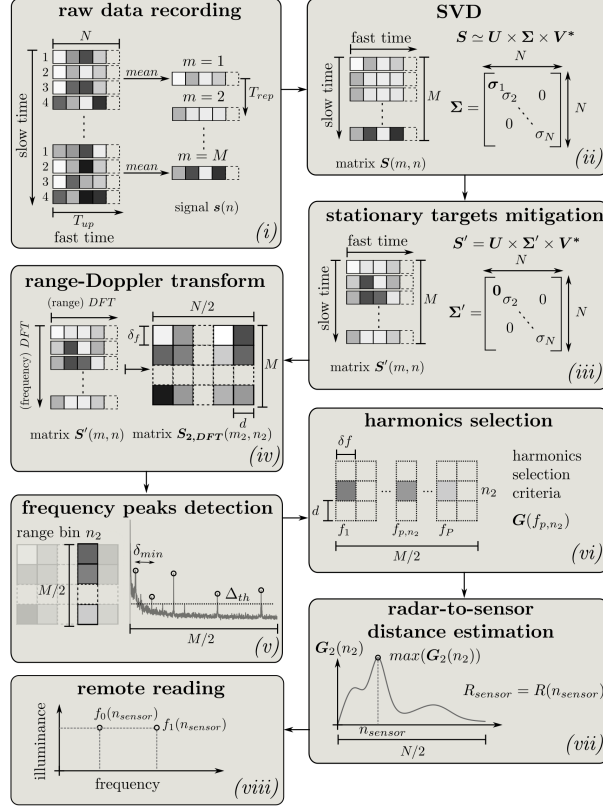
6

Figure 3: The different steps of the proposed range-Doppler imaging algorithm.

$S_{2,DFT}(m_2, n_{sensor})$ are derived. The detected harmonics $f_{p,n_{sensor}}$ are used to determine the illuminance of the light that illuminates the mechanical sensor.

# 3 Material and Method

## 3.1 Experimental Setup

The schematic of the experimental setup is displayed in Fig. 4a. The radar used in the experiment is a 24GHz FM-CW radar manufactured by Silicon Radar (*SiRad Easy*, see [15]). Parameters of the transmitted signal are similar to those described in Section 2.2. The maximal input power is 6dBm (around 4W) and transmitting and receiving antennas are V-polarized patch antenna arrays. The power gain of the radar receiver amplifier is set to 56dB. The passive mechanical sensor is a Crookes radiometer illuminated by a light source. A second variable and identical light source, called here the *reference light*, illuminates the probe of a luxmeter (model *CA1110*). The distance between the probe of the luxmeter and the reference light is 5cm. The 2x2cm$^2$ pans of
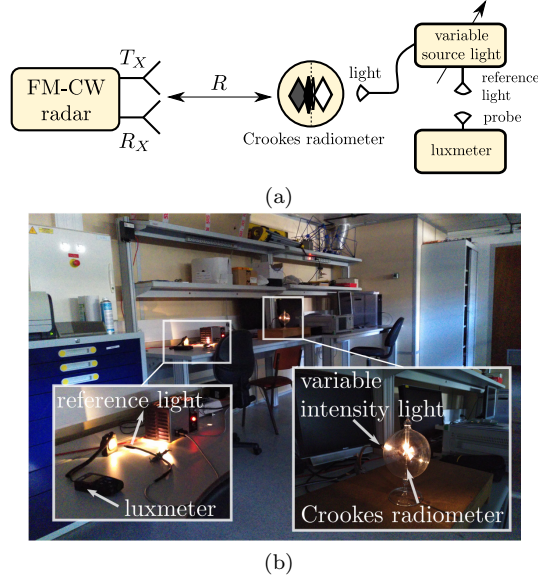
Figure 4: (a) Schematic of the experimental setup. (b) Second scenario where the Crookes radiometer is at a distance of 3.5m from the radar in a room of our Laboratory.

the Crookes radiometer are inclined by few degrees as described in Section 2.2. The sensor is interrogated by the radar for two different scenarios:

*(i)* the first measurement is performed in an anechoic chamber and the radar-to-sensor distance $R$ is set to 2.1m;

*(ii)* the second measurement is performed in the room of our Laboratory and the radar-to-sensor distance $R$ is set to 3.5m, as depicted in Fig. 4b. Measurements are finally performed for various controlled light illuminances. For each measurement, minimal, maximal and averaged illuminances are recorded.

## 3.2   Measurement Results

Measurements are performed for the two scenarii and the range-Doppler imaging algorithm described in Section 2.3 is applied on the measured radar data. In order to refine the estimation of the radar-to-sensor distance $R$, the matrix $S(m,n)$ is averaged with a window of varying size $n_w$ (from $n_w$=1 to $n_w$=10) along the slow time axis. The final estimated radar-to-sensor distance is derived from the highest occurrence among 10 estimations. In Fig. 5 is displayed the typical range-Doppler image obtained after applying the step *(iv)* of the algorithm. In this measurement, the Crookes radiometer is illuminated with an illuminance of about 1500lx in the room of our Laboratory. Black to white colors represent low (-80dB) to high (-20dB) echo levels. Blue crosses are frequency peaks detected after applying the step *(v)* of the algorithm. Green crosses are harmonics detected among all the frequency peaks (step *(vi)* of the algorithm).
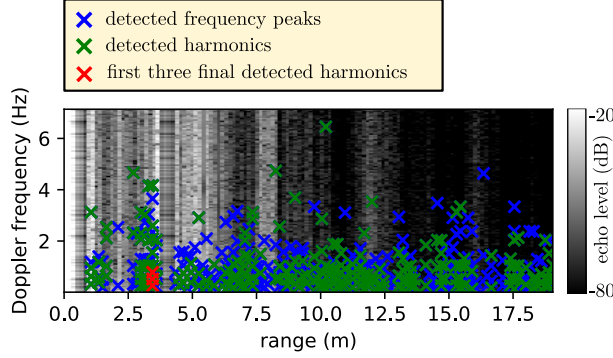
8

Figure 5: Range-Doppler image obtained when the Crookes radiometer is illuminated by a light source of illuminance about 1500lx in a room of our Laboratory at 3.5m. Final detected harmonics are represented by the red crosses.

Red crosses are the three first harmonics $f_2$, $f_4$ and $f_6$ detected after estimating the distance of the Crookes radiometer (step *(vii)* of the algorithm). For both scenarii, the distance $R$ is estimated with a precision of $\pm 2d$. The performance of the detection depends on the harmonics selection described in step *(vi)* as well as the signal-to-noise ratio of range-Doppler images.

After estimating the radar-to-sensor distance, we apply the step *(viii)* of the algorithm on the Doppler spectrum $S_{2,DFT}(m_2, n_{sensor})$. Harmonics are measured and plotted in Fig. 6 for various illuminances obtained in the anechoic chamber and in the room of our Laboratory. Black, blue and green markers represent respectively the first, second and third detected harmonics. Up and down triangles are minimal and maximal measured illuminances, whereas crosses are averaged measured illuminances. As expected, the frequency of the detected harmonics increases as the illuminance increases. We note that most of the frequencies are found to be $f_2$, $f_4$ and $f_6$ since the pans of the Crookes radiometer do not have a perfect $\frac{\pi}{2}$-rotational symmetry (see Section 2.2). A linear model based on the measurements of the first detected harmonic $f_2$ in the anechoic chamber as a function of the averaged illuminance is now proposed (see black dashed line in Fig. 6a). We obtain the correlation coefficient $R^2$=0.973, the sensitivity $\alpha$=10807lx/Hz and the intercept $\beta$=-1013lx. We extend the validity of the linear model for different harmonics, as follows:

$$I_k = \frac{2\alpha f_k}{k} + \beta \qquad (7)$$

where $I_k$ denotes the illuminance and $k$=1,2,... is the rank of the corresponding harmonic. The linear model is plotted in Fig. 6 for harmonics $f_4$ (blue dashed line), $f_6$ (green dashed line) and $f_8$ (red dashed line). Most of the detected harmonics match to the linear model for the two scenarii. We note that some harmonics expected to follow the $f_6$ model correspond in fact to the $f_8$ model, because $f_6$ peaks might have not been detected (see explanations in Section 2.2).
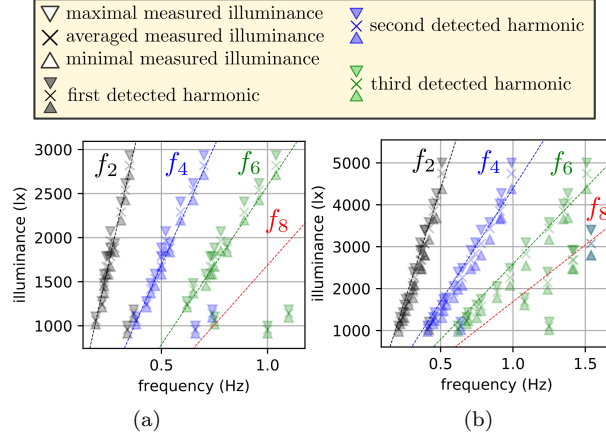
9

Figure 6: Measured illuminance as a function of the frequency of detected harmonics (a) in anechoic chamber with a Crookes radiometer located at 2.1m from the radar and (b) in room of our Laboratory with a Crookes radiometer located at 3.5m from the radar.

Resolution of the measurement depends on the resolution frequency $\delta_f$=3.2E-2Hz. If we consider the linear model of eq. (7), the illuminance is given with a resolution $\delta I_k = \frac{2\alpha\delta_f}{k}$. For harmonics $f_2$, $f_4$ and $f_6$, we have respectively $\delta I_2$=346lx, $\delta I_4$=172lx and $\delta I_6$=116lx. We observe a small offset between linear models and measurements in Fig. 6b. It is explained by variations of the distance between the reference light and the probe of the luxmeter. Measurements of the irradiance (in $W/m^2$) instead of illuminance (in lx) may remove this offset. We also observe that the gap between minimal and maximal values (down and up triangles) of the illuminance increases with the averaged illuminance. This effect is caused by the variability of the used light source. Anyway, these primarily measurement results are very encouraging. They pave the way to the design of new class of wireless passive sensor solutions for the remote sensing in cluttered stationnary environments based on the mechanical transduction principle.

## 4 Conclusion

In this paper, we showed that the long-range interrogation of mechanical sensors embedded in cluttered environments is possible from using a range-Doppler imaging algorithm. As they use mechanical transduction, such sensors do not require electronic chip and/or power supply, and do not need the challenging design and fabrication of electromagnetic transducers. We estimated wirelessly the reading range and the rotation speed of centimeter-size pans at radar-to-sensor distance of 3.5m in a cluttered environment. The proposed range-Doppler imaging technique may be applied to remotely measure other physical quantities,

10

such as pressure of temperature, in cluttered stationary environments by taking advantage of the mechanical transduction principle.

# References

[1]  R. Nair et al. "A humidity sensor for passive chipless RFID applications". In: *IEEE Int. Conf. RFID Technol. and Appl.* 2012, pp. 29–33.

[2]  D. Henry, H. Aubert, and P. Pons. "Radar Imaging Approach for Zero-Power Millimeter-Wave Wireless Sensors". In: *IEEE Int. Conf. RFID Technol. and Appl.* 2019, pp. 89–94.

[3]  O. Rance et al. "RCS magnitude coding for chipless RFID based on depolarizing tag". In: *IEEE Int. Microw. Symp.* 2015, pp. 1–4.

[4]  V. Palazzi et al. "A novel compact harmonic RFID sensor in paper substrate based on a variable attenuator and nested antennas". In: *IEEE Int. Microw. Symp.* 2016, pp. 1–4.

[5]  M. Pereira da Cunha et al. "Wireless harsh environment SAW array system for power plant application". In: *IEEE Int. Ultrason. Symp.* Sept. 2014, pp. 381–384. DOI: 10.1109/ULTSYM.2014.0094.

[6]  D. Henry et al. "Classification of Radar Echoes for Identification and Remote Reading of Chipless Millimeter-wave Sensors". In: (2020). in press.

[7]  T. T. Thai et al. "Novel Design of a Highly Sensitive RF Strain Transducer for Passive and Remote Sensing in Two Dimensions". In: 61.3 (2013), pp. 1385–1396.

[8]  S. Bouaziz et al. "Novel Microfluidic Structures for Wireless Passive Temperature Telemetry Medical Systems Using Radar Interrogation Techniques in Ka-Band". In: 11 (2012), pp. 1706–1709.

[9]  Osborne Reynolds. "The Dimensional Properties of Matter in the Gaseous State". In: *Nature* 19.489 (Mar. 1879), pp. 435–437. DOI: 10.1038/019435a0.

[10] M. Azadi et al. "Demonstration of Atmospheric-Pressure Radiometer With Nanocardboard Vanes". In: (2020), pp. 1–7.

[11] H. Lim et al. "Radar Cross Section Measurements of a Realistic Jet Engine Structure with Rotating Parts". In: *J. of Electromagn. Waves Appl.* 25.7 (2011), pp. 999–1008. DOI: 10.1163/156939311795253993.

[12] A. Meta, P. Hoogeboom, and L. Ligthart. "Range Non-linearities Correction in FMCW SAR". In: *IEEE Int. Symp. Geosci. Remote Sens.* 2006, pp. 403–406.

[13] S. O. Piper. "Receiver frequency resolution for range resolution in homodyne FMCW radar". In: *Conf. Proc. Nat. Telesyst. Conf.* June 1993, pp. 169–173. DOI: 10.1109/NTC.1993.292991.

[14] J. J. M. de Wit, A. Meta, and P. Hoogeboom. "Modified range-Doppler processing for FM-CW synthetic aperture radar". In: 3.1 (2006), pp. 83–87.

[15]  *Evalkits - Silicon Radar Wiki.* https : / / siliconradar . com / wiki / Evalkits. Accessed: 2020-09-29.